Journal of Hydrology 603 (2021) 127034

Contents lists available at ScienceDirect

Journal of Hydrology

journal homepage: www.elsevier.com/locate/jhydrol

Influence of urban forms on long-duration urban flooding: Laboratory experiments and computational analysis

Xuefang Li [a,*], Sébastien Erpicum [a], Emmanuel Mignot [b], Pierre Archambeau [a], Michel Pirotton [a], Benjamin Dewals [a]

[a] Hydraulics in Environmental and Civil Engineering (HECE), University of Liège (ULiège), Belgium
[b] LMFA, CNRS-Université de Lyon, INSA Lyon, Ecole Centrale de Lyon, Université Claude Bernard Lyon 1, France

ARTICLE INFO

This manuscript was handled by C. Corradini, Editor-in-Chief

Keywords:
Urban flooding
Urban forms
Flood-resilience
Laboratory model
Numerical modelling

ABSTRACT

Water-sensitive urban design is an integral part of flood risk management. Based on computational modelling, we investigated the influence of various urban forms on flooding severity at the level of an urban block and for the case of long-duration urban flooding. The upstream flow depths, downstream discharge partition and flow exchange through the urban forms were examined. The results indicate that one urban characteristic has an overwhelming influence on the flow variables: the conveyance porosity in the main flow direction is by far more influential than the conveyance porosity in the normal direction or the number of streets. Such anisotropic effect was not pointed in recent similar studies, and it hints at practical guidelines for sustainable urban planning in practice. Moreover, the computational model was verified against laboratory observations, which constitute a novel valuable dataset for the validation of other urban flooding models.

1. Introduction

1.1. Need for flood resilient urban design

Worldwide, urban flooding causes huge economic losses and a high number of fatalities (Kreibich et al., 2019). The impacts of urban flooding are rising as a result of rapid urbanization and more frequent extreme rainfall events (Chen et al., 2015; Muis et al., 2015; Yin et al., 2015). This trend puts urban flood risk modelling and management as a global priority (Guo et al., 2020; Nkwunonwo et al., 2020; Rosenzweig et al., 2021)

Experience has shown that effectively mitigating urban flood risk is only possible if the scope of urban flood risk management is extended well beyond traditional approaches such as upgrade of flood defenses and urban drainage systems (La Loggia et al., 2020; Rosenberger et al., 2021). Among other aspects, concepts such as *water-sensitive urban planning* or *sponge cities* are increasingly considered as an integral part of urban flood risk management (Qin, 2020; Yin et al., 2021). Löwe et al. (2017) suggest that flood-resilient urban planning may be economically more efficient than upgrading the drainage system in a context of uncertain future climate. Similarly, based on multiple urbanization scenarios at the regional level, Mustafa et al. (2018) pointed out that future flood risk will be strongly influenced by spatial planning policies. The arrangement of buildings is a major component of urban planning. The resulting *urban forms* affect not only flood vulnerability but also flood hazard. Indeed, the layout of buildings in floodplains alters the flow paths (Leandro et al., 2016), so that flood hazard is changed both in magnitude and in terms of spatial distribution (upstream depths and downstream discharges). Lin et al. (2020) showcased the importance of geometric parameters characterizing the arrangement of buildings on pluvial flooding hotspots in a real-world urban district (Shenzhen, China). Hence, the influence of urban forms on flooding is an important aspect of flood-resilient urban design (Yin et al., 2021).

1.2. Existing experimental and numerical studies on urban forms

Urban flooding was extensively studied over the last few years (Teng et al., 2017; Mignot et al., 2019; Tesema and Abebe, 2020); but the influence of urban forms on flooding has received relatively little attention. Table 1 lists existing computational and experimental studies dedicated to the impacts of variations in the arrangement of buildings on flow patterns. As detailed below, the most widely investigated parameters include building density (Cea et al., 2010; Huang et al., 2014; Guillén et al., 2017; Dong et al., 2021), street or building orientation

* Corresponding author.
E-mail addresses: xuefang.li@uliege.be, li.xuefang2016@gmail.com (X. Li).

https://doi.org/10.1016/j.jhydrol.2021.127034
Received 14 June 2021; Received in revised form 26 August 2021; Accepted 30 September 2021
Available online 7 October 2021

Table 1
Previous experimental and numerical research on the influence of urban forms on urban flooding.

Reference	Lab	Num.	Type of building layout [1]	Building density	Building or street orientation	Street width	Aligned or staggered buildings	Others	Number of tested building arrangements	Steady vs. unsteady [2]	Source of flooding [2]	Analyzed flow variables [4]	Objectives [3]
Huang et al. (2014)	✓	✓	GO	×					7	S	RF	Flow depth (~27%)	Validation + Processes
Guillen Ludena et al. (2017)	✓		GO	×					9	S	RF	Forces on obstacles (~100%)	Processes
Dong et al. (2021)	✓	✓	GO	×					3	UN	DB	Upstream flow depth (~insignificant)	Validation + Processes
Herbich and Shulits (1964)	✓		GO	×		×			11	S	RF	Flow depth (~5% – 25%)	Processes
Soares-Frazão and Zech (2008)	✓	✓	GO		×				2	UN	DB	Flow depth (~5–12%)	Validation + Processes
Tomiczek et al. (2016)	✓		GO			×			3	UN	SW	Flow depth (~7% –20%) + pressure on obstacles (up 70%)	Processes
Velickovic et al. (2017)	✓	✓	GO		×	×			5	S	RF	Flow depth (~4% – 12%)	Validation + Processes
Goseberg (2013)	✓		GO		×		×		4	UN	SW	Flow depth (~8% –23%) + Velocity	Processes
Testa et al. (2007)	✓		GO				×		2	UN	DB	Flow depth (~20%)	Validation
Cea et al. (2010)	✓	✓	GO	×			×		8	UN	PF	Runoff hydrograph (peak discharge:~11% –33%)	Validation
Isidoro et al. (2013)	✓		GO					×	5	UN	PF	Runoff hydrograph (peak discharge:(~9%-45%)	Processes
Löwe et al. (2017)		✓	RD	×					2	S	PF	Flooded area, flood damage, flood risk (up to 2 times)	Processes
Bruwier et al. (2018)		✓	SN	×	×	×		×	2,000	S	RF	Flow depth (up to 2 times)	Processes
Bruwier et al. (2020)		✓	SN						2,000	S	PF	Flow depth (~28% – 43%), water storage (~13%-60%) and runoff hydrograph	Processes
Mustafa et al. (2020)		✓	SN + RD						3 case studies, numerous layouts	S	RF	Flow depth (up to 29%)	Processes
Present study	✓	✓	SN	×		×		×	19	S	RF	Flow depth, discharge partition, 2D velocity field	Validation + Processes

[1] GO: regular grid of obstacles representing building blocks at the district level; RD: real district; SN: street network
[2] Flow regime: US: unsteady; S: steady. Type of flooding: DB: upstream dam failure; RF; river flooding; PF: pluvial flooding; SW: submersion wave
[3] Research objectives are classified into two categories depending on the main purpose of varying urban forms in the research *(i)* Validation: providing experimental data for validating computational models; *(ii)* Processes: understanding the influence of urban forms on flow processes
[4] Flow variables which were measured / simulated when varying the building arrangements. The values provided in brackets represent an estimated range of the magnitude of the influence of urban form on the corresponding variable (either provided directly in the original paper, or estimated based on results displayed in the original paper)

(Herbich and Shulits, 1964; Soares-Frazão and Zech, 2008; Velickovic et al., 2017), street width (Tomiczek et al., 2016; Velickovic et al., 2017) and building positioning (aligned vs. staggered) (Testa et al., 2007; Cea et al., 2010; Goseberg, 2013; Isidoro et al., 2013). Based on an outdoor scale model of a river valley, in which a dam break-induced flood wave was simulated, Testa et al. (2007) performed pointwise measurements of flow depth evolution for two distinct building arrangements (aligned and staggered buildings). In a laboratory setup operated with steady inflow, Velickovic et al. (2017) investigated the distribution of flow depths for five arrangements of buildings, which differed by the orientation of the streets with respect to the direction of approaching flow and by the street widths. Huang et al. (2014) measured flow depths in a series of laboratory experiments involving building arrangements characterized by seven different building coverage ratios. In these three studies, no other flow variable than flow depth was analyzed. Tomiczek et al. (2016) investigated the influence of the spacing between buildings on turbulence and hydrodynamic loads on buildings during a tsunami wave submersion. Recently, laboratory observations by Dong et al. (2021) suggested a lower influence of the building arrangement compared to the effect of urban drainage in the case of a dam break wave. However, the setup was limited to a single street and only two values of building density were tested. Two experimental studies investigated the influence of building arrangements on pluvial flooding. Cea et al. (2010) tested eight different building arrangements and measured the runoff hydrograph at the outlet of the urban area. Their analysis focused on the validation of two computational models. Isidoro et al. (2013) considered a fixed building density, but they varied the rooftop connectivity. A substantial influence on runoff hydrographs was observed, with reductions in peak discharges of the runoff hydrograph when the building rooftops are more clustered.

Overall, in all previous experimental studies, the velocity fields and discharge partitions within the built area were not comprehensively investigated. Moreover, the number of tested configurations remained generally limited, which restrains the possibility of reaching conclusive results of broad interest. Particularly, no experimental study so far performed a systematic analysis of relatively complex urban forms, involving street intersections of several types.

A limited number of studies used computational modelling to bring insights into the influence of urban forms on flooding. For a case study in Melbourne (Australia), Löwe et al. (2017) estimated future flood risk under various scenarios of urban development and rain intensities. They highlighted that water-sensitive urban design appears as effective as other flood adaption strategies (e.g., rainwater harvesting tanks or increase of the pipe network capacity) for reducing flood hazard. However, the so-called water-sensitive urban design of Löwe et al. (2017) shows essentially a lower building coverage (i.e. more multi-storey apartment buildings), while subtler effects of urban forms on flooding mechanisms were not investigated. Based on computations involving 2,000 synthetic arrangements of buildings, Bruwier et al. (2018) analyzed the sensitivity of flow depths with respect to nine urban geometric parameters (typical street length, width, and curvature, building coverage, etc.) for the case of river flooding. Their main findings suggest (i) a dominating influence of the district-level conveyance porosity (ratio of voids in a cross-sectional area over the whole area), and (ii) that more “fragmented” urban forms (i.e. larger and more numerous spaces in-between buildings) tend to reduce flooding severity. Based on the outcomes of Bruwier et al. (2018), Mustafa et al. (2020) demonstrated a procedure for the automatic design of flood-sensitive urban layouts, by combining an optimization algorithm, an efficient hydraulic model and procedural modelling for the parameterized generation of urban layouts.

Bruwier et al. (2020) extended the analysis to the case of pluvial flooding, showing that in this particular case urban density (building coverage) is a suitable explanatory variable for predicting the influence of building arrangement on flow depth, water storage and runoff hydrograph.

These computational studies showcase the substantial influence of urban characteristics on flow variables during urban flooding; but they involve specific flow patterns in complex urban layouts, for which neither field nor laboratory validation data exist. Moreover, comprehensive research involving thousands of urban forms

(Bruwier et al., 2018, 2020) allowed deriving statistical regressions between urban parameters and flood danger; but the flow patterns were too complex to enable direct physical interpretation and a sound understanding of the flow processes at stake. Therefore, we aim here at conducting a more in-depth systematic analysis of a limited number of geometric parameters under more controlled flow conditions (i.e. simpler settings).

1.3. Objective

In the present research, we combine computational modelling and laboratory experiments to study the influence of urban forms on flow characteristics over a building block (i.e. the area encompassed between four intersecting streets). The experimental tests allow detailed validation of the computational model based on a restricted number of representative urban configurations, while the computations enable a more systematic assessment of the influence of urban forms on flow processes. A series of nineteen urban forms were considered. They were generated by varying the arrangement of buildings as well as the number and width of minor streets inside a building block. These variations either lead to a change in the conveyance porosity of the building block, or to a change in the number of minor streets, with the aim of disentangling the relative importance of the different effects.

We performed two-dimensional numerical simulations for all considered urban forms and typical river flooding conditions. The results obtained for five out of nineteen urban forms were verified in dedicated laboratory experiments. The laboratory dataset includes pointwise flow depth measurements upstream of the urban block, discharge partition at the street outlets as well as surface flow velocity measured by Large Scale Particle Image Velocimetry (LSPIV).

Section 2 describes the overall methodology, while the validation of the computational model is detailed in Section 3. The numerical results are presented in Section 4 and discussed in Section 5, and conclusions are drawn in Section 6.

2. Data and methods

Our overall methodology consists of four steps: (i) define urban forms; (ii) for a limited number of them, verify the numerical model by comparing against experimental data; (iii) perform systematic numerical simulations to assess the influence of urban forms on the flow variables; (iv) conclude on the influence of urban forms on flow variables.

The considered urban forms are introduced in Section 2.1 and the flooding scenario in Section 2.2, together with the examined flow variables. The numerical model is briefly presented in Section 2.3, while Section 2.4 provides a description of the laboratory experiments.

2.1. Urban forms

To assess the influence of urban forms on flow characteristics, we considered a part of a synthetic urban district. As shown in Fig. 1, it involves two main streets along one direction and two main streets in the normal direction, forming four crossroads (with three- or four-branches). The width of the main streets is noted b and was kept constant. Various urban forms were defined inside the central rectangular area surrounded by the four main streets. The size of this area is $L_y = 6.4\,b$ along direction x , and $L_x = 2.4\,b$ along direction y. These values are plausible and they correspond to the dimensions of the laboratory setup used for validating the numerical model (Section 2.4).

2.1.1. Independent parameters

Four independent dimensionless parameters were used to define the urban forms considered in the rectangular central area:

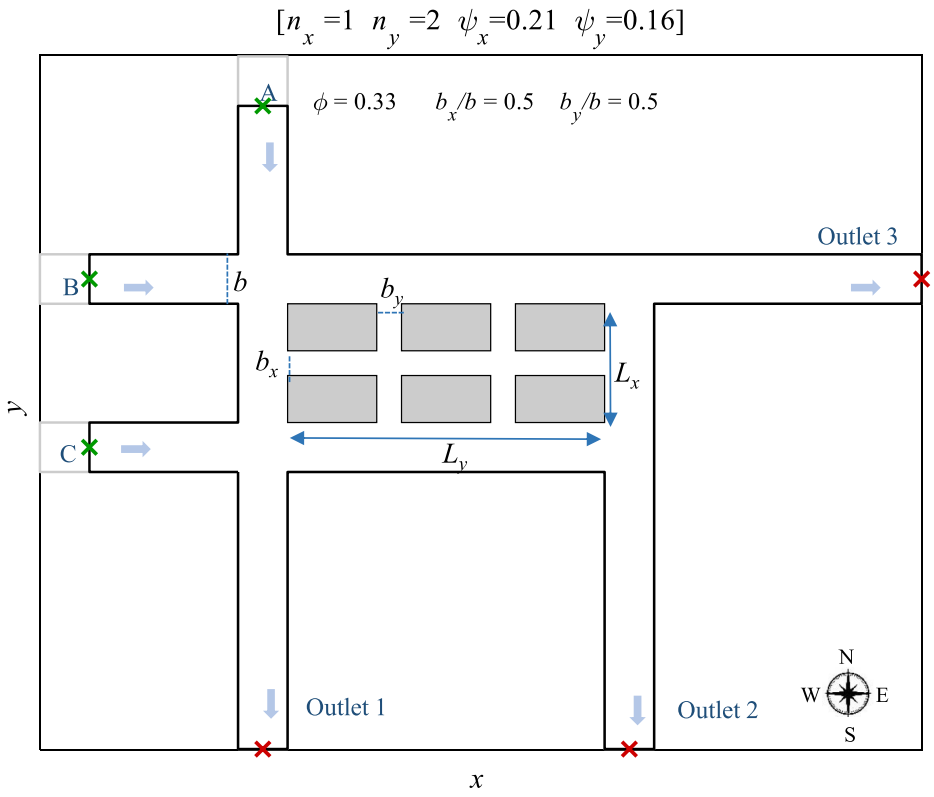

Fig. 1. Geometry of the reference urban form. Upstream flow depths were measured at the positions showed by green crosses (×). Red crosses (×) indicate the positions where the downstream boundary condition was prescribed. Bold black lines sketch the domain used for numerical modelling. (For interpretation of the references to color in this figure legend, the reader is referred to the web version of this article.)

- n_x and n_y, the number of minor streets aligned along directions x and y;
- the conveyance porosities $\psi_x = (b_x n_x) / L_x$ and $\psi_y = (b_y n_y) / L_y$, where b_x and b_y denote the widths of the minor streets.

All minor streets aligned along one direction were assumed of identical width. The value of b_x and b_y can then be computed from the values selected for the four independent parameters [n_x, n_y, ψ_x, ψ_y]. Similarly, the storage porosity ϕ of the central area is not another independent parameter as it can be evaluated as a function of ψ_x and ψ_y:

$$\phi = 1 - (1 - \psi_x)(1 - \psi_y) = \psi_x + \psi_y - \psi_x\psi_y \quad (1)$$

The motivation for selecting parameters n_x, n_y, ψ_x and ψ_y to control the considered urban forms results from a trade-off between realism of the generated urban forms, and simplicity of the analyses. As such, the present research complements previous studies (e.g., Bruwier et al., 2018, 2020) which account for a broader range of urban parameters (such as street curvature and orientation) but lead to a level of complexity in the generated urban forms which makes impossible to unveil direct causative relationships between each urban parameter and the flow characteristics.

2.1.2. Reference configuration

One urban form was selected as a reference, and all other urban forms were obtained by changing a single independent parameter (n_x, n_y, ψ_x or ψ_y) while keeping the three others unchanged. The urban form represented in Fig. 1 corresponds to the reference configuration. It includes one minor street along direction x ($n_x = 1$) and two minor streets along direction y ($n_y = 2$). In this configuration, the width of all minor streets was set to half the width of the main streets: $b_x = b_y = b / 2$. The conveyance porosities ψ_x and ψ_y are 0.21 and 0.16, respectively. Although arbitrary to some extent, the reference configuration was selected for its plausibility considering the extent and aspect ratio of the central area, and a realistic ratio between the widths of the main streets and the minor streets.

2.1.3. Systematic variations of the independent parameters

Fig. 2 displays the set of urban forms obtained by starting from the reference configuration and varying one independent parameter at a time. The corresponding parameters are given in Table 2. The numbers of minor streets, n_x and n_y, were varied systematically between 0 and 4. Six different values between 0 and 0.63 were considered for the conveyance porosity ψ_x, and six others for ψ_y between 0 and 0.47. Two additional, extreme configurations were included in the analysis: one with a closed central area (CO) and one with an open space in the central area (CE).

2.2. Flooding scenario

The flow depth is prescribed as the downstream boundary condition at each street outlet, and the inflow discharge is prescribed as the upstream boundary condition at each street inlet. To simplify the definition of the considered flooding scenario, the downstream flow depth h_0 is set equal at the three street outlets, and the inflow discharge Q_{in} is also set to the same value at the three inlets. Therefore, a "flooding scenario" is here entirely defined by one downstream flow depth and one inflow discharge. The focus was set on urban flooding conditions representative of floodplains of lowland rivers.

To determine a plausible inflow discharge Q_{in}, we introduced a characteristic Froude number F defined based on the input data, i.e. the flow depth h_0 (0: outlet), the inflow discharge Q_{in} and the width b of the main streets:

$$F = \frac{Q_{in}}{b h_0 \sqrt{g h_0}} \quad (2)$$

This represents the Froude number which would be observed at the street outlets if the outflow discharge was distributed uniformly between the three outlets, as it is at the inlets. By assuming a value for F, the inflow discharge Q_{in} at each inlet can be determined. Here, the flow was

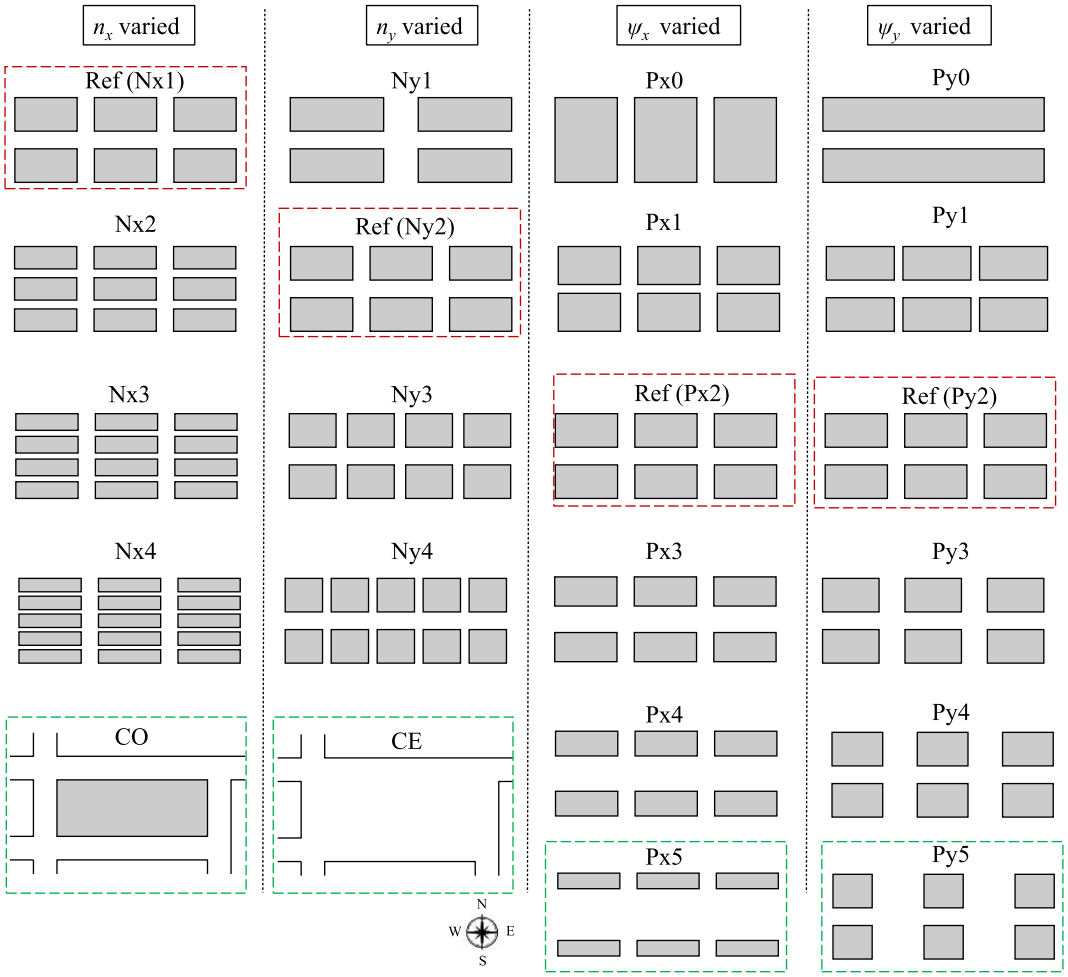

Fig. 2. Urban forms considered in the numerical simulations. The configurations highlighted by a dashed red or green box were also studied experimentally (red boxes correspond to the reference configuration). (For interpretation of the references to color in this figure legend, the reader is referred to the web version of this article.)

Table 2
Parameters characterizing the considered urban forms.

Configuration	n_x	n_y	ψ_x	ψ_y	b_x / b	b_y / b	ϕ
CO	–	–	0	0	0	0	0
CE	–	–	1	1	–	–	1
Ref (Nx1)	1	2	0.21	0.16	0.5	0.5	0.33
Nx2	2	2	0.21	0.16	0.25	0.5	0.33
Nx3	3	2	0.21	0.16	0.17	0.5	0.33
Nx4	4	2	0.21	0.16	0.125	0.5	0.33
Ny1	1	1	0.21	0.16	0.5	1	0.33
Ref (Ny2)	1	2	0.21	0.16	0.5	0.5	0.33
Ny3	1	3	0.21	0.16	0.5	0.33	0.33
Ny4	1	4	0.21	0.16	0.5	0.25	0.33
Px0	1	2	0	0.16	0	0.5	0.16
Px1	1	2	0.1	0.16	0.25	0.5	0.24
Ref (Px2)	1	2	0.21	0.16	0.5	0.5	0.33
Px3	1	2	0.31	0.16	0.75	0.5	0.42
Px4	1	2	0.42	0.16	1	0.5	0.51
Px5	1	2	0.63	0.16	1.5	0.5	0.68
Py0	1	2	0.21	0	0.5	0	0.21
Py1	1	2	0.21	0.08	0.5	0.25	0.27
Ref (Py2)	1	2	0.21	0.16	0.5	0.5	0.33
Py3	1	2	0.21	0.23	0.5	0.75	0.39
Py4	1	2	0.21	0.31	0.5	1	0.46
Py5	1	2	0.21	0.47	0.5	1.5	0.58

assumed relatively slow, with a characteristic Froude number F of 0.2, consistent with typical values observed in floodplains of lowland rivers.

2.3. Numerical model

For all configurations displayed in Fig. 2, numerical simulations were carried out with the same computational model and procedure as presented by Li et al. (2020). Based on a finite volume technique, the model solves the 2D shallow-water equations on a Cartesian grid with a depth-averaged k-ε turbulence model (Erpicum et al., 2009). The bed shear stress is estimated by Darcy–Weisbach formula. A steady inflow discharge was prescribed at each inlet and equal flow depths were prescribed at the outlets. The mesh spacing was set so that the grid includes 40 computational cells over the width of the main streets. Results of mesh sensitivity analysis are displayed in Supplement (Figure S1).

Some computed flow fields show small periodic fluctuations, with a period considerably longer than the computational time step. Although their amplitude is extremely small (below 1 % for discharge, and even smaller for flow depths), the displayed results were time-averaged over a duration sufficiently long compared to the period of the fluctuations. This is further detailed in Li et al. (2020).

2.4. Laboratory experiments

2.4.1. Experimental setup

Laboratory experiments were performed to validate the computational model. The tests were conducted in the Laboratory of Engineering

Hydraulics at the University of Liège, Belgium. The experimental setup represents the urban configuration shown in Fig. 1, and is exactly the same as detailed by Li et al. (2021), except for the urban forms. The bottom is flat and made of smooth PVC plates. The roughness height k_s is estimated at 5×10^{-5} m. The side-walls are vertical and made of 0.3 m high Plexiglass plates. The width of all streets is $b = 0.2$ m, representing a prototype street width of 10 m by applying a horizontal scale factor e_H of 50 ($e_H = L_p / L_m$ with L_p and L_m representing horizontal dimensions at prototype and model scale, respectively). The building blocks placed in the central part of the models are made of smooth Plexiglass plates of 0.15 m in height.

The flow in the physical model is steady and water is recirculated in a closed-loop system, involving a bottom tank of 2.4 m^3. In all tests, the inflow discharge was set at the same value in each inlet. Flow depths at the downstream end of the streets were regulated with adjustable weirs and they were set at the same value at the three outlets.

2.4.2. Downscaling of flooding scenario

Downscaling the prototype-scale flooding scenario defined in Section 2.2 to the scale of the laboratory setup consists in determining the values of the flow depth to be prescribed experimentally at the street outlets and the discharge to be prescribed at the street inlets in the laboratory model. Scaling the flow depth from prototype conditions to the laboratory setup is performed by defining a vertical scale factor e_V ($e_V = H_p / H_m$ with H_p and H_m representing vertical dimensions at prototype and model scale, respectively).

In urban flooding, the horizontal dimensions (street width and length ~ 10 –10^3 m) are way larger than the vertical ones (flow depth $\sim 10^{-1}$ –1 m). Therefore, opting for a vertical scale factor e_V equal to the horizontal one e_H leads generally to a too low Reynolds number in the scale model (leading to spurious effects due to water viscosity), as well as particularly low flow depth (and, hence high relative measurements errors and spurious effects of surface tension). Consequently, opting for a geometrically distorted scale model offers several benefits (higher Reynolds number, lower relative measurement errors), as detailed by Li et al. (2019) and Li et al. (2020). Here, we selected a vertical scale factor $e_V = 5$, which corresponds to a geometric distortion ratio $d = e_H / e_V$ of 10. Considering the flow depth at street outlet at the prototype-scale be 0.5 m, this leads to a flow depth prescribed at the model street outlets equal to $h_0 = 0.1$ m.

To achieve similarity between the physical model and the prototype, the characteristic Froude number F was kept the same in the scale model as in the prototype. This enables determining the inflow discharge Q_{in} at each street inlet in the scale model with $e_H = 50$ and $e_V = 5$:

$$Q_{in} = F\ b\ h_0 \sqrt{g h_0} = 3.96\ l/s \tag{3}$$

The effect of model geometric distortion is further discussed in Section 5.3.

2.4.3. Measurement techniques

The three inflow discharges were monitored independently by three electromagnetic flowmeters (SIMENS-MAG 5100 W), with an accuracy of 0.5%. Upstream flow depths were measured with ultrasonic sensors (Microsonic: Mic + 35/IU/TC), with an accuracy of 1 mm. To evaluate the partition of the outflow discharge between the streets, the flow at each outlet was collected in a straight horizontal measurement channel (width of 0.2 m and length of 1.5 m), equipped with a 90° triangular sharp-crested weir. The outflow discharge in each measurement channel was estimated by means of calibrated rating curves based on the hydraulic head in the measurement channels, as described by Li et al. (2021). To account for periodic fluctuations in the measured flow depths, the signal from each ultrasonic sensor was recorded for a duration of 120 s at a frequency of 100 Hz. This enables characterizing both the time-averaged value and the standard deviation of flow depths. All measurements were repeated twice to ensure reproducibility of the results (Figure S2 in Supplement). The uncertainties affecting the measurement of the outflow discharge at each street outlet were discussed in detail by Li et al. (2021). They are in the range 0.5% − 1.5%.

Surface velocity was measured by means of Large-Scale Particle Image Velocimetry (LSPIV), which is a non-intrusive and widely applied technique for field and laboratory measurements (Muste et al., 2008, 2014; Peltier et al., 2014; Naves et al., 2019). Here, a commercial camera LUMIX-GH4 (resolution of 1920 × 1080 pixels and recording rate of 25 fps) was placed 2 m above the laboratory model. Sawdust with a diameter ranging between 1 mm and 3 mm was used as a tracer. Its light color contrasts well with the PVC model bottom. Based on a convergence test (Figure S7 in Supplement), the duration of each video was fixed at 60 s (i.e. 1500 images). As detailed in Supplement (Figure S4 to S6), the experimental model was covered by combining movies recorded from several viewpoints. This enables minimizing hidden areas and increases the spatial resolution (to 1 mm/pixel).

The recorded image sequences were processed with software Fudaa-LSPIV (Le Coz et al., 2014), which was extensively applied in the field (Zhu and Lipeme Kouyi, 2019) and laboratory studies (Legout et al., 2012; Mejia-Morales et al., 2021). Three main steps were followed:

- Step 1: a 3-D orthorectification of the images was applied based on 10 to 20 ground reference points (GRP) positioned at three different elevations ($z = 0$ m, $z = 0.15$ m and $z = 0.3$ m, see yellow points in Fig. 3).
- Step 2: the surface velocity was calculated by tracking the path of particles in a predefined 'Interrogation Area' (IA) over a selected 'Search Area' (SA), as detailed by Legout et al. (2012). The considered IA extended over 20 pixels (i.e. 0.02 m × 0.02 m) (Legout et al., 2012). The size of the SA along each direction was adjusted as a function of the estimated magnitude of the maximum velocity along the respective directions. The spacing interval of the points where the velocity was calculated is 0.01 m, leading to 20 measurement points along the width of the main streets.
- Step 3: surface velocity fields were post-processed by Fudaa-LSPIV to filter out anomalous values, based on thresholds applied on the velocity components.

The surface velocity close to the sidewalls of the model was deemed unreliable because the tracers were slowed down at the contact with the sidewall. Therefore, computed surface velocities in a narrow strip of 1 cm along the sidewalls were discarded.

3. Assessment of the computational model

The computational model was first assessed by comparison against laboratory experiments. Comparisons focus first on the flow depths measured upstream of each street (points A, B, C), and on the outflow discharge at each outlet (Section 3.1). Next, similarities and differences between the computed depth-averaged flow velocity and the measured surface flow velocity are also discussed (Section 3.2).

3.1. Inlet flow depths and partition of outlet discharges

For the five measured configurations CE, CO, Ref, Px5 and Py5 (Fig. 2 and Table 2), the computed and observed upstream flow depths are shown in Fig. 4a. The standard deviations of measured and simulated flow depths among the different configurations are of the order of 0.7 mm and 0.001 mm, respectively. The difference between computed and observed values reaches a maximum of 1 mm, which is the best possible agreement given the experimental uncertainties (~1 mm). The quality of the agreement does not differ significantly from one geometric configuration to the other.

In three of the tested configurations (CO, Ref and Py5), the portion of the total discharge reaching each of the three street outlets (noted Q_R) varies in a relatively narrow range when the geometric configuration is

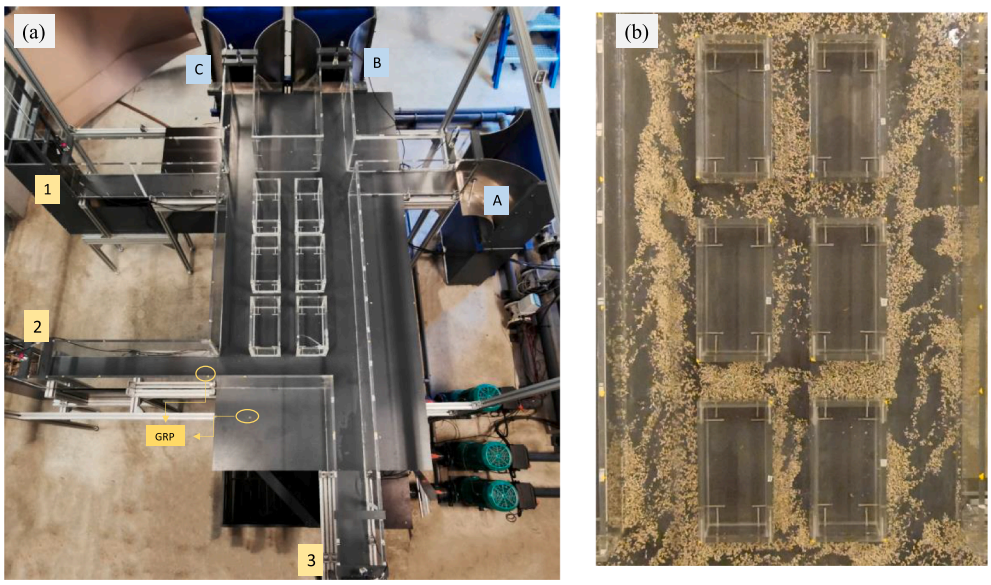

Fig. 3. (a) Physical model of a street network, yellow points represent Ground Reference Points (GRP); (b) snapshot of a LSPIV video frame. (For interpretation of the references to color in this figure legend, the reader is referred to the web version of this article.)

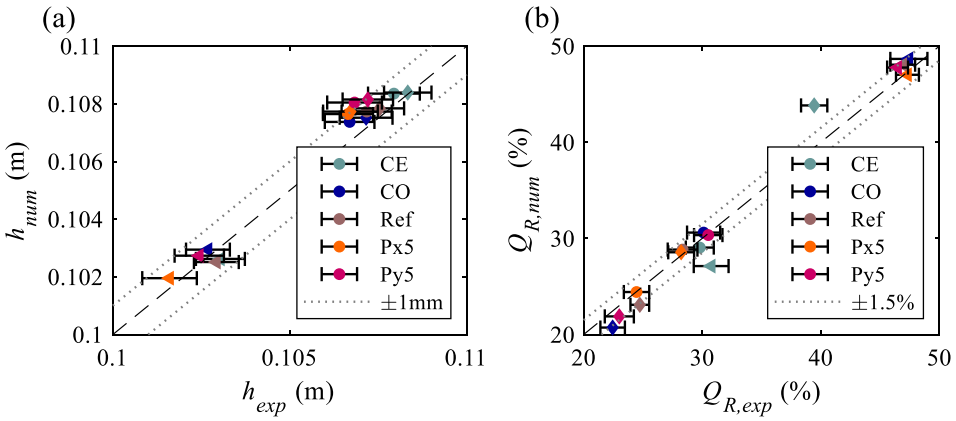

Fig. 4. (a) Comparison between computed (num) and measured (exp) flow depths upstream of each inlet (green point in Fig. 1). Symbols ●, ◆ and ▲ represent the flow depths at inlets A, B and C, respectively. (b) Comparison between computed and measured partitions of outflow discharge at the street outlets. Symbols ●, ◆ and ▲ refer respectively to outlets 1, 2 and 3. (For interpretation of the references to color in this figure legend, the reader is referred to the web version of this article.)

changed: between 28.5 and 30.5 % at outlet 1, between 22.5 and 25 % at outlet 2, and between 46.5 and 47.5 % at outlet 3 (Fig. 4b). Outlet 3 collects the highest portion of water as it is connected to inlets A and B by a single straight street. Outlet 2 drains the lowest amount of water because it is the most distant from the inlets. For all configurations except CE, the transfer of water in the west-east direction (evaluated as $Q_2 + Q_3$) is four times higher than the transfer in the north–south direction (evaluated as $Q_1 + Q_2 - Q_{in}$). In configuration CE, this ratio is close to two.

In configuration Px5, the portion of the flow reaching outlet 2 (28 %) is substantially higher than in configurations CO, Ref or Py5, at the expense of outlet 1 (24.5 %, compared to 29 % - 30 % for the three other configurations). This results from the high conveyance porosity ψ_x of Px5, leading to more water originating from inlets A and B to be conveyed towards outlet 2.

In these four configurations (CO, Ref, Py5 and Px5), the difference between computed and observed portions of discharge at the street outlets remains below 2 percentage points (pp), as can be seen in Figure S3 in Supplement. As for the inlet flow depths, this difference is comparable to the uncertainty affecting the experimental estimation of the outflow discharges (Section 2.4). As a result, the obtained agreement between computational and experimental results is again the best possible given the accuracy of the laboratory setup

In configuration CE (i.e. open space in the central area), the partition of the outflow discharge between outlets 2 and 3 differs considerably from that observed in the four other configurations. The highest portion of outflow discharge is collected at outlet 2, which is the outlet receiving the least water in configurations CO, CE and Py5 (Fig. 4b). In configuration CE, the absence of obstacles in the central area enables a strong flow crossing this area diagonally from inlets A and B towards outlet 2. The computational model succeeds in capturing this change in the partition of the outflow discharge, but it tends to slightly overestimate the measured discharge increase at outlet 2 and decrease at outlet 3 (Figure S3). The difference between computed and observed portions of outflow discharge reaches 4 pp. Overall, for most urban configurations, the differences between the numerical predictions and the experimental observations do not exceed the experimental accuracy, both for the flow depths at the street inlets and for the discharge partition between the street outlets. Only in configuration CE, the difference between the computed and observed portions of outflow discharge reaches up to 4 pp, which is higher than the experimental uncertainty. This aspect is further discussed below based on the velocity fields.

3.2. Flow velocity

Fig. 5 shows the measured surface velocity, the computed depth-averaged velocity, as well as the difference between these two quantities. The difference is normalized by a reference velocity (0.2 m/s), defined as the velocity which would be observed at the street outlets if

the outflow discharge was distributed evenly between the three outlets.

Since the observed and computed quantities do not correspond to the same flow variable (surface vs. depth-averaged velocity), there is no reason to expect a perfect agreement between the two. Indeed, 3D flow structures downstream of street intersections are known to induce deviations between surface and depth-averaged velocities (Li and Zeng, 2010; Mignot et al., 2013). Nonetheless, a high degree of (dis)similarity between the two quantities may hint at a (low) high overall level of confidence in the numerical predictions and may help with interpreting the (dis)agreement between observed and computed flow depths at street inlets and flow partition at street outlets.

In general, the patterns of computed depth-averaged velocity are found very similar to the patterns of observed surface velocity (Fig. 5). In particular, in the inlet sections, the difference between the two does not exceed 5 %, i.e. 0.01 m/s. This may be considered as a partial validation of the accuracy of our LSPIV technique.

Similarly, the computed depth-averaged velocities and the observed surface velocities in the contraction zones immediately downstream of

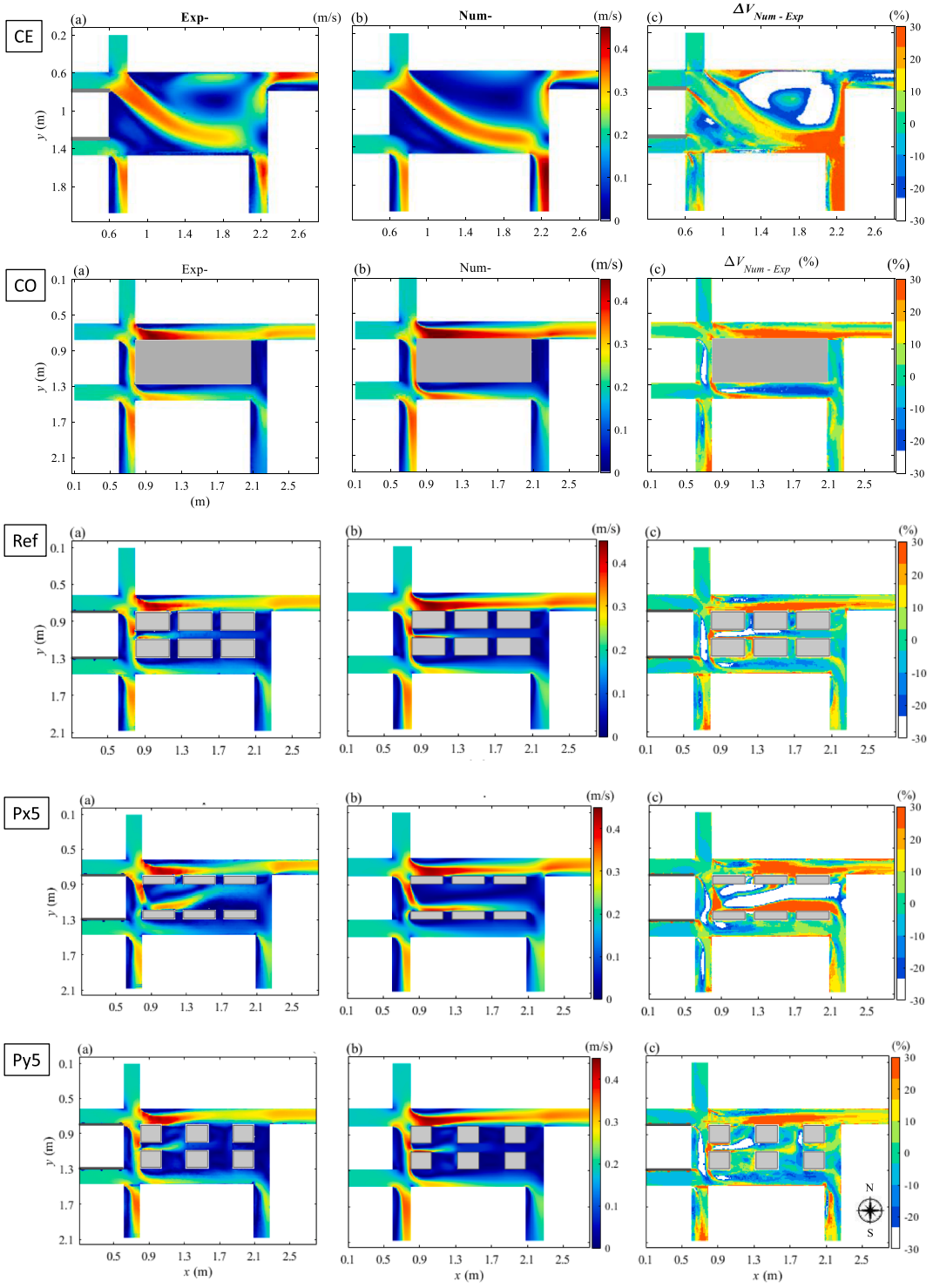

Fig. 5. Velocity field (time-averaged) in five geometric configurations: (a) measured surface velocity; (b) computed depth-averaged velocity; (c) normalized difference between computed and measured values.

the street intersections are also very close. This is shown in Figure S9 (in Supplement) which displays the cross-sectional velocity profiles at $x = 0.8$ m and $x = 1$ m (corresponding to the contraction zone) for street B3 (Fig. 1).

Further downstream (i.e. for $x \geq 1.4$ m), the differences between the velocity profiles tend to grow, suggesting that the recirculation lengths in the measured surface velocity and the computed depth-averaged velocity differ. Downstream of the contraction zones, the computed flow shows a more concentrated wall jet than in the observations, leading to local differences between computations and observations of the order of 30 % of the reference velocity (Fig. 5, and Figure S9 in Supplement). It is possible that such differences stem from the different physical natures of the observed and computed flow variables, i.e. difference between surface and depth-averaged velocities downstream of street intersection (El Kadi Abderrezzak et al., 2011; El Kadi Abderrezzak and Paquier, 2009; Li and Zeng, 2010; Mignot et al., 2013). Among others, Luo et al. (2018) and Li and Zeng (2010) found a larger flow velocity close to the bottom than at the surface downstream of crossroads, which is consistent with a higher depth-averaged velocity than the surface velocity as obtained here.

The cumulative distribution function (CDF) of the differences between computed depth-averaged velocity and observed surface velocity is displayed in Fig. 6. For configurations CO, Ref and Py5, the magnitude of the difference between the two quantities is in the range [– 10 %, 10 %] over 60 % of the flow domain and in the range [– 30 %, 30 %] over 90 % of the flow domain.

In configurations Px5 and CE, the CDF reveals stronger deviations. As shown in Fig. 5, for configuration Px5, the shape of the jet in the central part of the block differs between the observations and the computations. In the former case, the jet reattaches first against the obstacles located in the southern part of the central area, and at mid-length it reattaches to the obstacles located in the northern part. In contrast, in the simulations, the jet remains reattached to the southern obstacles. We consider as unlikely that this difference results from an actual deviation between depth-averaged and surface velocities, but it hints more likely at a limitation of the 2D computational model.

For configuration CE, the jet in the observed surface velocity field shows more dispersion than in the computations, and the observed large recirculation is more active in the observations than in the computations (Fig. 5c). The higher simulated velocity field close to outlet 2 is consistent with the overestimation of the outflow discharge at outlet 2 (Fig. 4b). Again, these differences are more likely to point at a limitation of the 2D model when applied to a wide open area than to reflect a real deviation between surface and depth-averaged velocity fields.

3.3. Flow in the minor streets

Fig. 7 provides a close look at the measured and computed flow fields in the minor streets for configurations Ref, Px5 and Py5. Empty arrows in Fig. 7 indicate the direction of net exchange between the minor and main streets. For the experiments, we determined this direction based on the visualization of the tracers motion in the recorded videos. The net flow exchange direction of numerical results is determined with the sign (positive / negative) of exchange discharges (see details in Figure S12 in Supplement).

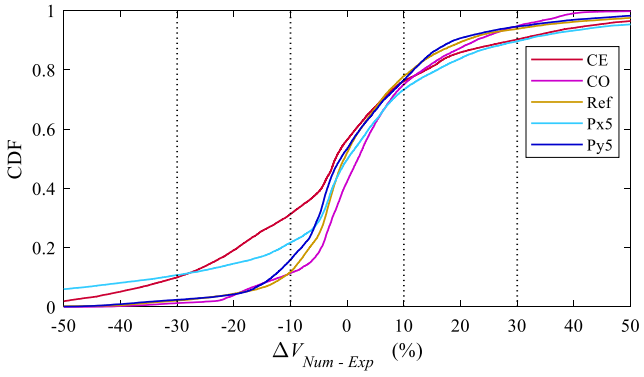

Fig. 6. Cumulative distributions of the bias between measured and simulated velocities in the configurations tested experimentally.

In most cases, the net exchange flow direction and the pattern of flow recirculation agree between the computations and the observations. Substantial differences occur in two cases: *(i)* minor streets in which the net flow exchange is very small, and therefore difficult to detect based on the tracers motion; and *(ii)* in configuration Px5, for which the main jet trajectory is inaccurately represented in the computations. As a consequence, the rotation of small recirculations in the eastern minor streets is reversed in the numerical predictions compared to the observations.

Overall, computed depth-averaged velocity and observed surface velocity are very similar, particularly in the inlet sections as well as in the vena contracta. In contrast, downstream of contraction zones, the computed jet remains more concentrated at the sidewall than in the observations. Also, in two configurations (Px5 and CE), the trajectories of jets are not accurately captured by the computations. In the next section, we present a systematic assessment of the influence of urban forms on flow variables, while keeping in mind the possible limitations of the computational model.

4. Results

Based on computations, we detail here the influence of urban forms on the upstream flow depths, the discharge partition at the outlets, and the exchange discharge between the central area and the adjacent main streets. The upstream flow depths and discharge partition at the outlets were selected for their ability to unveil upstream–downstream impacts of a particular urban form. Indeed, the flow depths at the inlets reflect the influence of the tested urban forms on the severity of flooding further upstream, while the discharge partition indicates how the tested urban forms may affect the distribution of flooding hazard further downstream. Finally, the magnitude of the exchange discharge between the central area and the main streets reveals information on the local flow processes within the considered urban block.

Note that Figure S10 in Supplement displays the computed velocity fields for all tested configurations.

4.1. Upstream flow depths and discharge partition

For all tested configurations, Fig. 8 shows the variation of the inlet flow depths and outlet discharge partitions, compared to the results obtained in the reference configuration:

$$\Delta h_i = \left(h_i - h_{\mathrm{Ref}}\right)/h_{\mathrm{Ref}} \qquad \text{and} \qquad \Delta Q_{R,i} = Q_{R,i} - Q_{R,Ref} \tag{4}$$

where subscript i refers to a particular urban form, subscript *Ref* refers to the reference configuration, h denotes the flow depth at a particular street inlet (A, B or C), and Q_R the fraction of the total outflow discharge which is drained by a particular outlet (1, 2 or 3).

Overall, Fig. 8a reveals that varying the urban forms does not change significantly the upstream flow depths (max. ~ 1 %). This results from the relatively low Froude number considered here. In contrast, the discharge partition at the street outlets is more sensitive to changes in the urban form, particularly at outlet 2, where it may vary by up to 6 pp compared to the reference configuration (Fig. 8b).

4.1.1. Effect of varying the number of minor streets

When the number n_x of minor streets along x is varied from 1 to 4 (the conveyance porosities ψ_x and ψ_y being kept constant) the outflow discharge at outlet 2 decreases monotonously, and vice-versa at outlet 1.

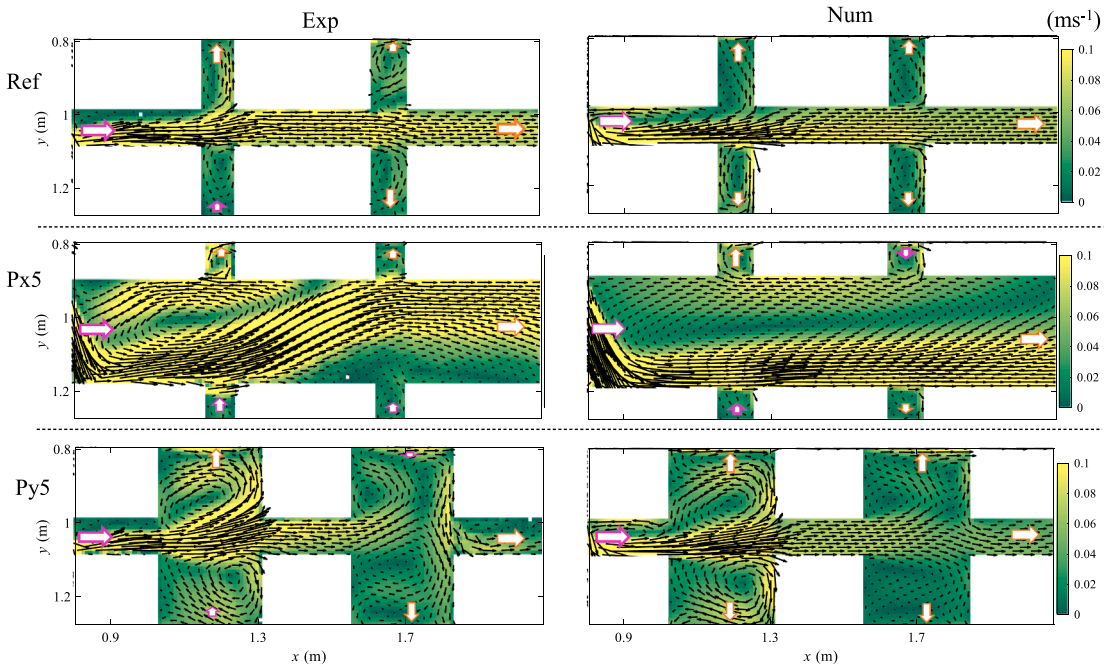

Fig. 7. Observed (left) and computed (right) flow fields in the minor streets in the central area. Empty arrows indicate the net flow exchange direction.

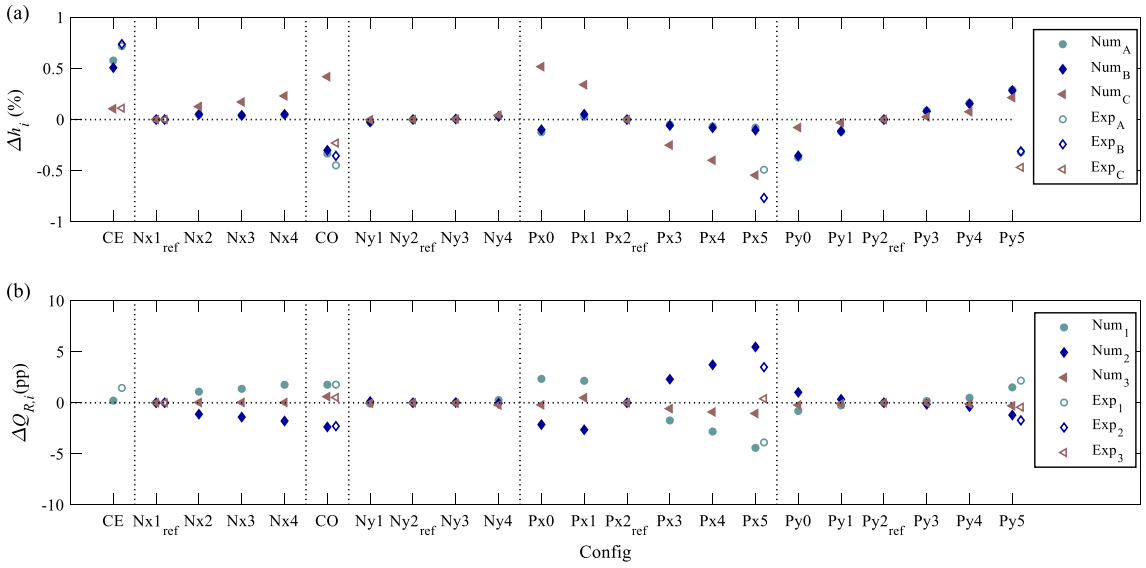

Fig. 8. (a) Variation of flow depth h at inlets, (b)Variation of flow discharge partition Q_R at outlets, compared with the results of the reference configuration. 'Empty symbols' represent the experimental measurements. For configuration CE, the variations in outflow discharge at outlets 2 and 3 extend beyond the range of the graph axis, as shown in Figure S11 in Supplement.

This reflects a higher flow resistance across the urban form along the x direction as n_x is increased, hence impeding the transfer of water from west to east towards outlet 2. This is consistent with an increase in flow resistance when a flow path of a given total width becomes fragmented into several narrower paths, leading to a larger total wetted perimeter for the same total cross-sectional area (ψ_x being constant). The results obtained with the highest number of minor streets (Nx4) are close to those of the extreme case CO, which involves an impermeable central area (Fig. 8b).

When the number n_y of minor streets along direction y is varied, the partition of the outflow discharge is barely affected. Indeed, flow recirculations occupy a large portion of those minor streets, as depicted in Fig. 5 and Fig. 7. Hence, irrespective of their number, the minor streets along y tend not to convey a significant amount of flow for all tested configurations (except CE). Fig. 5 also shows a considerable flow momentum in the main street linking inlet B to outlet 3. This tends to impede the deviation of water towards the minor streets aligned along direction y. Chen et al. (2018) showcased a similar effect in a synthetic network of streets, where the main streets were shown to act as flow "separators" inhibiting flow exchanges with minor streets on their sides.

The anisotropic geometry and boundary conditions considered here lead to a greater transfer of water from west to east than from north to south, and thus contrasting influences of n_x and n_y. The anisotropy of the setup is also the reason why the results of configurations CO and CE, which appear as two extremes from a geometrical perspective, do not provide an envelope of the results obtained with the other configurations in Fig. 8b.

4.1.2. Effect of varying the conveyance porosities

When the conveyance porosity ψ_x is varied, the partition of the outflow discharge is strongly modified (see configurations Px0 to Px5 in Fig. 8b). The range of the variation reaches up to 8 pp at outlet 2, which corresponds to an increase by one-third of the outflow discharge at this outlet when ψ_x is varied from 0 (Px0) to 0.63 (Px5). Conversely, the outflow at outlet 1 is reduced by 7 pp for the same change in ψ_x. As for n_x, modifying ψ_x influences directly the resistance to the dominating flow transfer, i.e. along the west-east direction: this transfer increases as ψ_x increases.

In contrast, changes in the conveyance porosity ψ_y (Py1 to Py5) have a milder influence on the outflow discharge partition. The ranges of variation are 3 to 5 times smaller than in the case of variations in ψ_x, with an opposite tendency: west-east transfers decrease as ψ_y increases.

4.1.3. Comparison with experimental results

Fig. 8 also displays the experimental results for the configurations tested in the lab (CE, CO, Ref, Px5 and Py5). The variations in flow depths at the inlets show some disagreements between the computations and the observations (e.g., for configurations CO, Px5 and Py5); but these effects lie all in the range of uncertainty of the experimental observations. For the outflow discharges, the computations and the observations lead in all cases to the same direction of change with regards to the reference. In configuration CO, the predicted and measured values of the change at all street outlets are even in perfect agreement, as shown by the corresponding symbols being perfectly aligned in Fig. 8b. For configurations Px5 and Py5, some differences are observed between experimental and numerical results, but they fall all in the range of the experimental uncertainties (~1 to 2 pp).

4.2. Exchange discharge with the central area

In addition to the flow depth at the street inlets and the discharge partition at the street outlets, we also examined the exchange discharges Q_E between the main streets and the central area that contains the minor streets, normalized by the total inflow discharge. This quantity represents the portion of the inflow discharge that is conveyed through the minor streets. It enables assessing the contribution of the central area to the overall flow conveyance depending on the urban form. To evaluate the exchange discharge Q_E, we summed up the integrals over the street width of the computed depth-averaged velocity profiles at each inlet of a minor street, considering only those with flow entering the central area ($Q_{E,in}$) or only those with flow leaving the central area ($Q_{E,out}$). Owing to mass conservation, $Q_{E,in} = Q_{E,out} = Q_E$. Details of the computation are given in Figure S12 (in Supplement). Unfortunately, the experiments do not give access to this information, since the observed surface velocity field is not sufficient to precisely infer the flow discharge in each street.

For each urban configuration involving minor streets, Fig. 9 shows the inlet and outlet exchange discharges, $Q_{E,in}$ and $Q_{E,out}$, and it highlights the contribution of each face (West, North, East, South) of the central area to the total exchange discharge $Q_{E,in}$ or $Q_{E,out}$. In all configurations except those in the group Px…, Q_E varies in a very narrow range: between 8 % and 11 % of the total inflow discharge. In contrast, when the conveyance porosity ψ_x increases, the exchange discharge increases dramatically, by up to two orders of magnitude: in configuration Px0, Q_E represents 0.2 % of the total inflow discharge, while it reaches 18 % of the inflow discharge in configuration Px5 ($\psi_x = 0.63$). This result explains to a great extent why the partition of outflow discharge is far more influenced by ψ_x than it is by the three other parameters n_x, n_y and ψ_y.

Irrespective of the urban configuration, water flowing through the central area enters mainly through the west face (Fig. 9a). It flows towards the east face, and to a lesser extent, towards the south and north faces (Fig. 9b). The partition of the exchange discharge $Q_{E,out}$ between these three faces is strongly dependent on the urban configuration (except for the group Ny). While Q_E increases monotonously when the conveyance porosity ψ_x increases, the evolution of Q_E with the other parameters (n_x, n_y and ψ_y) is slightly non-monotonous, due to several mechanisms. When the number of minor street n_x increases, the portion of the exchange flow entering the west face remains virtually constant, while the portion entering the east face evolves non-monotonously, leading to a non-monotonous evolution of the total exchange discharge. Moreover, when n_x is increased above 2, the discharge leaving the central area through the east face decreases, indicating a higher resistance faced by the flow passing through the urban form from west to east. This is consistent with the variation of the discharge partition with n_x. When ψ_y is varied from 0.08 to 0.47, the exchange discharges through the north and south faces are hardly modified (Fig. 9b), since the minor streets aligned along y axis are mostly occupied by large flow recirculations (Fig. 10). The computed flow fields in the minor streets are presented in Figure S17 (in Supplement) for all the configurations.

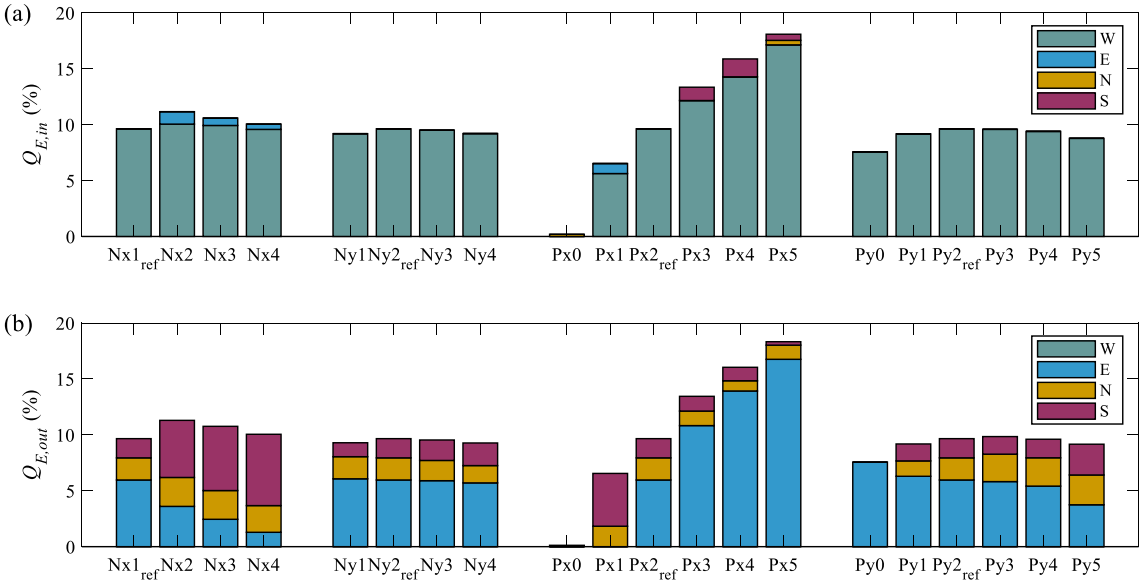

Fig. 9. Exchange discharge (normalized by the total inflow discharge), entering (a: $Q_{E,in}$) or leaving (b: $Q_{E,out}$) the central area. Labels W, N, E and S refer to faces of the central area: West, North, East or South (see also Figure S12).

5. Discussion

5.1. *Comparison with Bruwier et al. (2018)*

Although the building coverage (or storage porosity) of an urban district is certainly an important characteristic of urban forms, Bruwier et al. (2018) emphasized the stronger influence of the district-scale conveyance porosity compared to the storage porosity on the examined flow variables, particularly the upstream flow depths in the case of long-duration riverine flooding or runoff from upstream catchment. The present results are in agreement with Bruwier et al., (2018) conclusions. In particular, the storage porosity (ϕ, indicated in the last column of Table 2) alone does not enable predicting the direction nor the magnitude of the trends in the flow variables of interest, as demonstrated in Fig. 11. Hence, although the building coverage as used also by Dong et al. (2021), appears as a correct predictor of flow variables when the source of water is the rain falling over the considered urban area (Löwe et al., 2017; Bruwier et al., 2020), this parameter is not suitable when the water originates from riverine flooding or runoff volumes drained from further upstream of the considered urban area.

Our results point out the contrasting influence of the conveyance porosities ψ_x and ψ_y. The former affects directly the direction in which the strongest flow transfer occurs so that it has a considerably stronger effect on the flow variables, particularly the partition of the outflow discharge (Fig. 8b). This aspect could be highlighted here because our setup is non-isotropic, in the sense that the overall flow transfer along the north–south direction differs from the transfer in the west-east direction. In contrast, Bruwier et al. (2018) were unable to draw attention to these directional effects since their setup was isotropic as regards the boundary conditions and the outer geometry of the tested urban forms.

Another key point of Bruwier et al. (2018) work was that "more fragmented" urban forms (i.e. shorter street length and larger building side back) tend to reduce the flooding severity upstream of the considered urban area. However, it was not clear whether the concept of "fragmentation" refers to a number of voids, such as our parameters n_x and n_y, or the actual portion of a cross-sectional available for flow conveyance (similarly to ψ_x and ψ_y). Indeed, Bruwier et al. (2018) did not analyze the influence of modifying the number of streets while keeping the conveyance porosity constant: their urban forms were generated randomly, so that several parameters varied simultaneously. In contrast, based on our systematic approach, we have been able to disentangle the overwhelming influence of the conveyance porosity compared to that of the number of streets in a particular direction (Fig. 8).

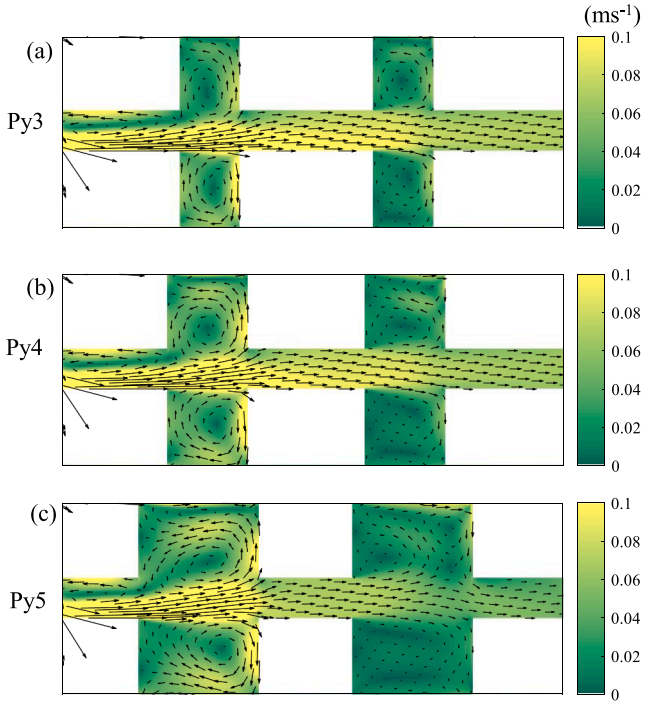

Fig. 10. Computed depth-averaged velocity in the central area for configurations Py3, Py4 and Py5.

5.2. *Effect of bottom and sidewall roughness*

Similarly to Li et al. (2020), all computational results presented in Section 4 were obtained by considering smooth bottom and side-walls: the roughness height was assumed equal to $k_s = 5 \times 10^{-5}$ m. To assess the influence of this assumption on the results, a series of computations was repeated with a considerably larger value for the roughness height: $k_s = 10^{-3}$ m. Considering a vertical scale factor $e_V = 5$ (Section 2.4), this value of k_s corresponds to 5 mm at the prototype scale, which is a plausible value for typical material encountered in real-world urban districts. These additional computations were carried out for configurations Px1, Ref (Px2), Px3, Px4 and Px5, which lead to the strongest variations in the flow characteristics.

The flow depths computed with $k_s = 10^{-3}$ m are systematically higher than those computed with $k_s = 5 \times 10^{-5}$, but the differences do not exceed 0.5 mm (Figure S22a). Similarly, the differences in the discharge partition for both roughness values are very small, below 1p.p. (Figure S22b). Besides, the variation of these two flow characteristics with the urban form (Fig. 12a-b) remains consistent with those obtained for the lower value of roughness (Fig. 8a-b). Finally, the roughness doesn't seem to have any substantial influence on the exchange discharge Q_E nor on its directional distribution, as can be inferred by comparing Fig. 12c-d with Fig. 9. This enables concluding that the findings presented in Section 4 are not altered when the value of the roughness height is varied.

5.3. *Extrapolation to the prototype scale*

Additional computations were performed to evaluate the validity of extrapolating to the real-world the findings obtained based on a reduced-scale model of urban flooding. When setting these computations, both the district geometry and the hydraulic boundary conditions were upscaled to the prototype scale, in line with Section 2.4. The focus was set on the series of configurations Px1, Ref (Px2), Px3, Px4, Px5, which shows the highest influence on the flow characteristics (Fig. 8 and Fig. 9). A roughness height $k_s = 0.005$ m was assumed.

As shown in Figure S18 in Supplement, the results remain very similar between the computations conducted for the reduced-scale model and those at prototype scale. Both the flow depths at the inlets and the discharge partitions at the outlets are consistent irrespective of the scale: at all inlets and outlets, the direction of change of these flow variables with ψ_x is not altered and, although not identical, the magnitudes of the variations are also similar at both scales (e.g., 1p.p. difference in terms of discharge partition). The same observations apply for the exchange discharges $Q_{E,in}$ and $Q_{E,out}$ in the five tested configurations (Figure S19), although the flow direction is reversed in some of the minor streets, but this corresponds to tiny contributions to the total exchange discharge (Figure S20). At prototype scale, for all values of ψ_x, the flow enters the central area through the north and west sides, and leaves this area through the south and east sides (Figure S21), whereas at the reduced-scale the flow direction in some of the minor streets varies with ψ_x. This difference results from the change in the flow aspect ratio between the reduced-scale model and the prototype scale, but it does not undermine the conclusions of the present study since the discharge flowing through these minor streets contributes little to the overall exchange flow.

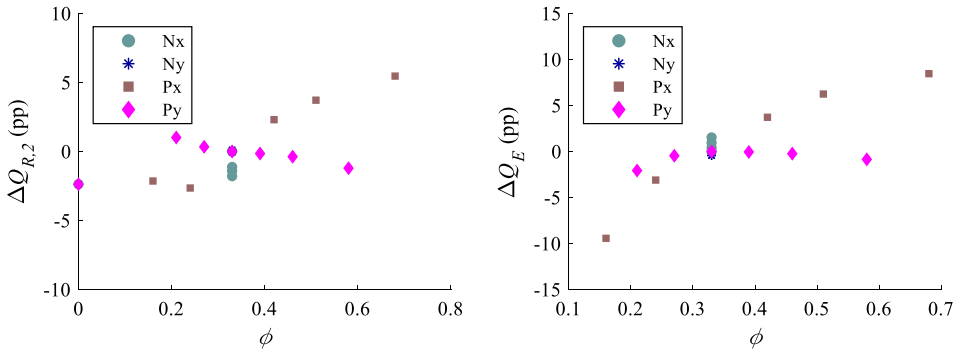

Fig. 11. Variation of flow discharge partition at outlet 2 ($Q_{R,2}$) and exchange discharge Q_E compared with the results of reference configuration, as a function of the storage capacity ϕ.

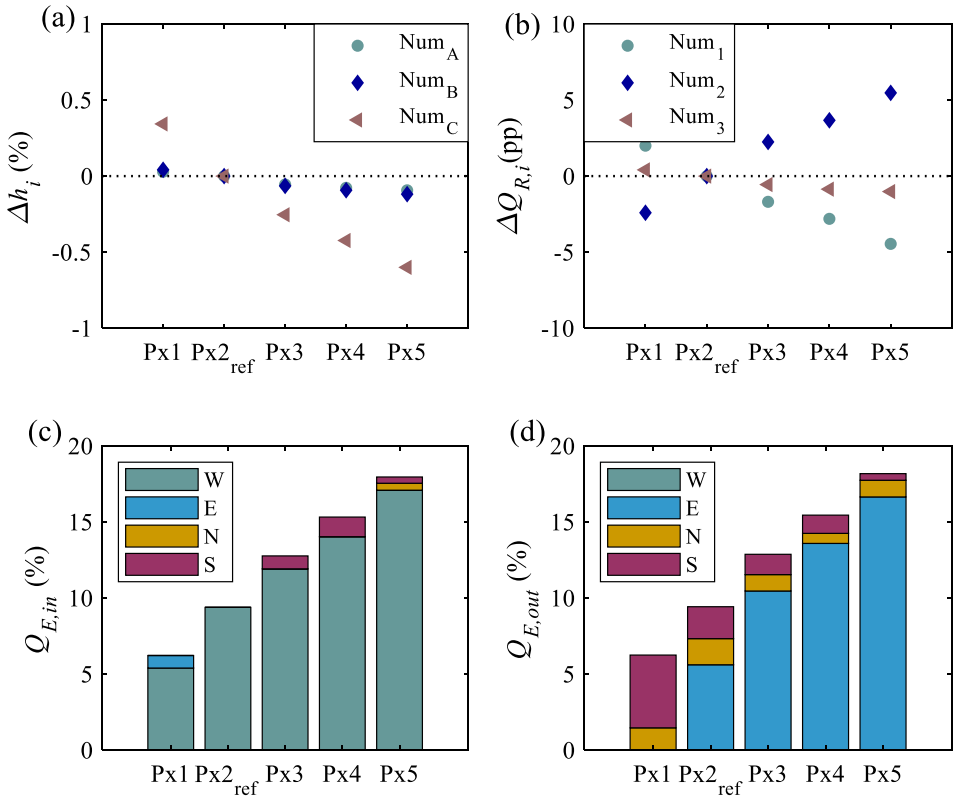

Fig. 12. Results with 'rough' model bottom with $k_s = 0.001$ m: (a) Variation of flow depth h at inlets, (b)Variation of flow discharge partition Q_R at outlets, compared with the results of the reference configuration; (c), (d) exchange discharge (normalized by the total inflow discharge) entering ($Q_{E,in}$) and leaving ($Q_{E,out}$) the central area.

5.4. Limitations of the study

This study contains some limitations. First, only a part of a synthetic street network was analyzed, together with a limited number of urban forms. Although the considered geometry was selected so that it includes a variety of crossroad types and building patterns, it is certainly not representative of all settings possibly encountered in real-world urban fabrics. This may limit the extrapolations of our findings to other practical situations. Conversely, the selected geometry, together with the hydraulic boundary conditions, has the merit of highlighting the non-isotropic behavior of asymmetrical urban districts.

Another limitation stems from the fixed hydraulic boundary conditions considered throughout the study. As detailed in Section 2.2, it was chosen representative of typical long-duration flooding conditions in floodplains of lowland rivers. Nonetheless, we believe that most conclusions would remain unchanged if the hydraulic boundary conditions were varied, particularly the ranking of the urban forms in terms of their influence on the flow variables. For instance, increasing the inflow discharge would mainly magnify the magnitude of the influence of the urban characteristics on the flow variables; but it would certainly not reverse the trends. This effect was shown by Arrault et al. (2016) based on a laboratory model of an urban district, in which the inflow discharge was varied over one order of magnitude.

The scaling chosen for the laboratory experiments, involving a geometric distortion of 10 (Section 2.4) could also be questioned. Note that, compared to the case of a geometrically undistorted model, the geometric distortion enables obtaining a Reynolds number in the laboratory model closer to that at prototype-scale, at the expense of altering the aspect ratio of the flow sections. It also reduces the relative importance of measurement uncertainties. Li et al. (2020) quantified the effects of

varying the geometric distortion for the case of configuration CO (Fig. 13a, b). Here, we repeated a similar analysis for the reference configuration (Ref). While the laboratory observations used in Section 3 were all based on a geometric distortion of 10, we repeated the measurements and computations with six other values of d, ranging between 1.6 and 12.5 (Fig. 13c, d). In both configurations (CO and Ref), the results are barely affected by the distortion ratio, provided that this ratio remains above 5. Only for $d < 5$, a substantial influence of d is observed due to a magnified effect of flow resistance as the geometric distortion, and hence the flow depths, are reduced. This leads to variations by up to 5 % of the inlet flow depths and by 10 pp of the outlet discharge. Moreover, the computational model captures reliably the influence of geometric distortion on the results, irrespective of the particular urban configuration (CO or Ref).

6. Conclusion

Based on experimental and computational modelling, we analyzed how flow variables (flow depths, discharge partition and velocity field) in urban flooding are influenced by a particular set of urban forms. The considered urban forms consist of a regular network of orthogonal streets. They are characterized by four parameters, which were systematically varied. The most striking result of the study is the overwhelming influence of just a single parameter (the conveyance porosity along the direction of dominating flow) compared to the three others (conveyance porosity in the normal direction, as well as the numbers of streets along each direction). This result stems from the anisotropy of the considered geometric and hydraulic setting, in which water transfer along one direction (west-east) is roughly four times stronger than along the normal direction (north–south). This effect was not revealed in similar recent studies (e.g., Bruwier et al. (2018)), which considered more isotropic geometric and hydraulic boundary conditions. It suggests also that, in the tested configurations, the building coverage (or building density), which is isotropic, is not a suitable predictor of the effect of urbanization on flooding.

From a practical perspective, this finding suggests that, when a preferential flow direction can be identified, new developments altering the conveyance porosity along this direction should be scrutinized with great care. This effect should act as a constraint in the design of new developments in floodplains. Vice-versa, the limited influence of the conveyance porosity and the number of streets along the direction normal to the main flow offer an opportunity for new developments which do not increase flooding severity, and may safely be constructed provided they are flood-proof themselves. Moreover, the relatively high conveyance porosity along the main flow direction should be ensured based on a limited number of flow paths (e.g., few wide streets, and not multiple narrower streets), as our analyses highlight that fragmenting a flow path into several ones (by increasing n_x) increases the flow resistance.

Detailed comparisons between laboratory observations and computational results are another key outcome of the present study. It reveals the ability of a 2D computational model to capture the most typical flow features of urban flooding in a street network. In contrast, more substantial deviations were pointed out between computations and observations in configurations CE and Px5, which involve an open area. For engineering practitioners, this result hints at the need for a critical assessment of computational predictions when open areas, such as large squares, are modelled in 2D. Furthermore, the experimental dataset collected here may prove valuable for the validation of other urban flood models, such as porosity models (Ferrari et al., 2019; Varra et al., 2019; Ferrari and Viero, 2020), in a broad range of urban settings.

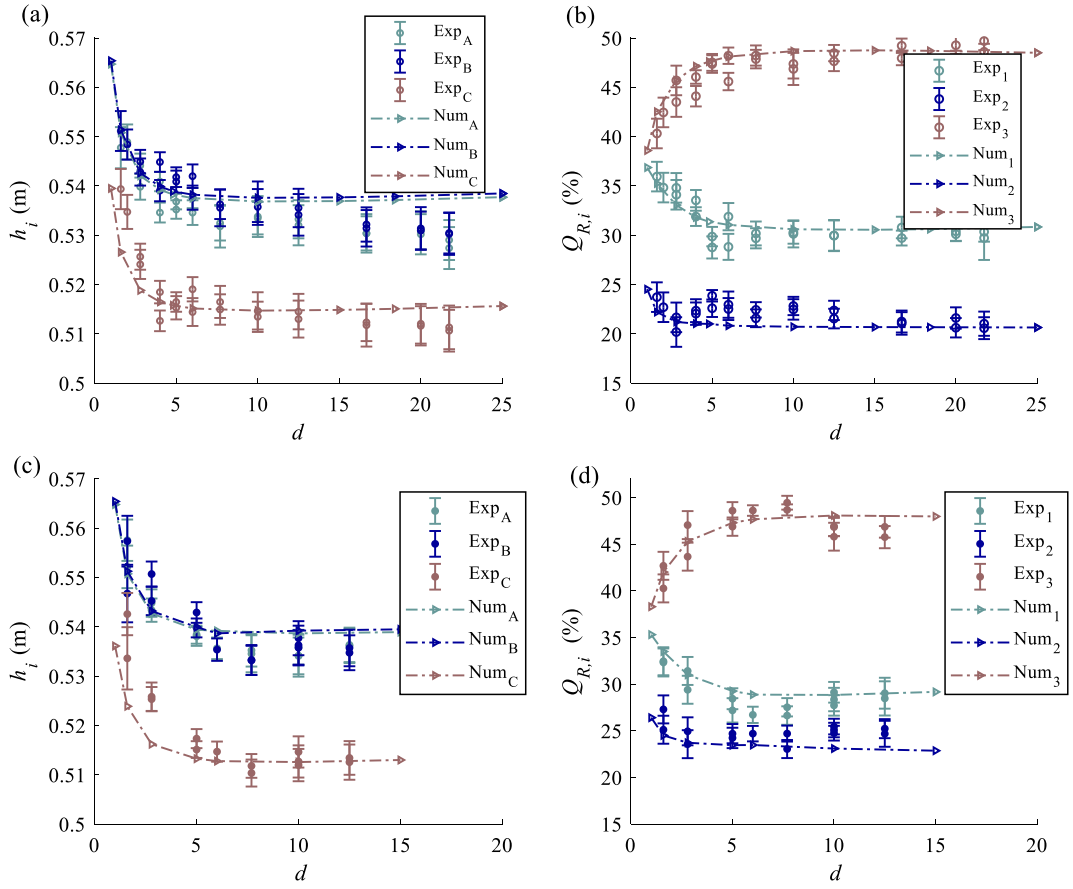

Fig. 13. Influence of geometric distortion d on observed and computed upscaled inlet flow depths (a, c) and outlet discharge partitions (b, d) in configurations CO (a, b) and Ref (c, d). Error bars show the standard deviation of measured time-series values.

Although the geometry and hydraulic boundary conditions considered here were selected to represent a variety of urban flooding conditions (e.g., various crossroads with three or four branches) while remaining sufficiently generic, they are certainly not representative of all urbanistic configurations which may arise in real-world urban areas (Dottori et al., 2013). Therefore, the present study should be complemented by the analysis of many more urban configurations and hydraulic scenarios, by means of a stochastic framework, as well as the study of real-world cases and data (e.g., Paquier et al. (2020)), including steeper terrain slopes and shorter flooding durations (El Kadi Abderrezzak et al., 2009). Similarly, further research is needed on the interplay between urban design and other flow controlling factors in urban flooding, such as surcharging urban drainage (Martins et al., 2018; Rubinato et al., 2018; Beg et al., 2020), flow intrusion into buildings (Mignot et al., 2020), green infrastructures (Rosenberger et al., 2021). The relative importance of these processes should be examined not only in light of the flow characteristics but also in terms of induced damage (Dottori et al., 2016; Molinari et al., 2020). Finally, novel methods such as 3D-virtual environments constitute another promising approach for assessing the influence of urban design on flood risk (Zhi et al., 2020).

Declaration of Competing Interest

The authors declare that they have no known competing financial interests or personal relationships that could have appeared to influence the work reported in this paper.

Acknowledgements

This research was funded by a fellowship from the “Fonds pour la formation à la Recherche dans l′Industrie et l′Agriculture” (FRIA, Belgium), as well as by a grant from “Fonds Spéciaux de la Recherche” (FSR) of the University of Liege. The support from the French National Research Agency (ANR) for the project DEUFI (ANR-18-CE01-0020) is also acknowledged. The authors gratefully acknowledge Miguel Angel Mejia-Morales for his insightful suggestions for LSPIV set-up and Prof. Jérôme Le Coz for his support of Fudaa-LSPIV. The authors are also grateful to the technical stuff of the laboratory, Maxime Mathieu, Grégory Thonard and Claude Lhermerout.

Experimental datasets and figures in .fig format are available on the repository Zenodo: https://doi.org/10.5281/zenodo.5243191, from which they will be freely accessible.

Appendix A. Supplementary data

Supplementary data associated with this article can be found, in the online version, at https://doi.org/10.1016/j.jhydrol.2021.127034.

References

Arrault, A., Finaud-Guyot, P., Archambeau, P., Bruwier, M., Erpicum, S., Pirotton, M., Dewals, B., 2016. Hydrodynamics of long-duration urban floods: experiments and numerical modelling. Natural Hazards and Earth System Sciences 16, 1413–1429.

Beg, M.N.A., Rubinato, M., Carvalho, R.F., Shucksmith, J.D., 2020. CFD Modelling of the Transport of Soluble Pollutants from Sewer Networks to Surface Flows during Urban Flood Events. Water 12.

Bruwier, M., Maravat, C., Mustafa, A., Teller, J., Pirotton, M., Erpicum, S., Archambeau, P., Dewals, B., 2020. Influence of urban forms on surface flow in urban pluvial flooding. Journal of Hydrology 582, 124493.

Bruwier, M., Mustafa, A., Aliaga, D.G., Archambeau, P., Erpicum, S., Nishida, G., Zhang, X., Pirotton, M., Teller, J., Dewals, B., 2018. Influence of urban pattern on inundation flow in floodplains of lowland rivers. Science of the Total Environment 622–623, 446–458.

Cea, L., Garrido, M., Puertas, J., 2010. Experimental validation of two-dimensional depth-averaged models for forecasting rainfall-runoff from precipitation data in urban areas. Journal of Hydrology 382, 88–102.

Chen, S., Garambois, P.-A., Finaud-Guyot, P., Dellinger, G., Mosé, R., Terfous, A., Ghenaim, A., 2018. Variance based sensitivity analysis of 1D and 2D hydraulic models: An experimental urban flood case. Environmental Modelling & Software 109, 167–181.

Chen, Y., Zhou, H., Zhang, H., Du, G., Zhou, J., 2015. Urban flood risk warning under rapid urbanization. Environmental Research 139, 3–10.

Dong, B., Xia, J., Zhou, M., Deng, S., Ahmadian, R., Falconer, R.A., 2021. Experimental and numerical model studies on flash flood inundation processes over a typical urban street. Advances in Water Resources 147, 103824.

Dottori, F., Di Baldassarre, G., Todini, E., 2013. Detailed data is welcome, but with a pinch of salt: Accuracy, precision, and uncertainty in flood inundation modeling. Water Resources Research 49, 6079–6085.

Dottori, F., Figueiredo, R., Martina, M.L.V., Molinari, D., Scorzini, A.R., 2016. INSYDE: A synthetic, probabilistic flood damage model based on explicit cost analysis. Natural Hazards and Earth System Sciences 16, 2577–2591.

El Kadi Abderrezzak, K., Lewicki, L., Paquier, A., Rivière, N., Travin, G., 2011. Division of critical flow at three-branch open-channel intersection. Journal of Hydraulic Research 49, 231–238.

El Kadi Abderrezzak, K., Paquier, A., 2009. Numerical and Experimental Study of Dividing Open-Channel Flows. Journal of Hydraulic Engineering 135, 1111–1112.

El Kadi Abderrezzak, K., Paquier, A., Mignot, E., 2009. Modelling flash flood propagation in urban areas using a two-dimensional numerical model. Natural Hazards 50, 433–460.

Erpicum, S., Meile, T., Dewals, B.J., Pirotton, M., Schleiss, A.J., 2009. 2D numerical flow modeling in a macro-rough channel. International Journal for Numerical Methods in Fluids 61, 1227–1246.

Ferrari, A., Viero, D.P., 2020. Floodwater pathways in urban areas: A method to compute porosity fields for anisotropic subgrid models in differential form. Journal of Hydrology 589, 125193.

Ferrari, A., Viero, D.P., Vacondio, R., Defina, A., Mignosa, P., 2019. Flood inundation modeling in urbanized areas: A mesh-independent porosity approach with anisotropic friction. Advances in Water Resources 125, 98–113.

Goseberg, N., 2013. Reduction of maximum tsunami run-up due to the interaction with beachfront development - application of single sinusoidal waves. Natural Hazards and Earth System Sciences 13, 2991–3010.

Guillen Ludena, S., Lopez, D., Mignot, E., Rivière, N., 2017. EXTREME FLOOD FLOW IN AN INCREASINGLY URBANIZED FLOODPLAIN: AN EXPERIMENTAL APPROACH.

Guillén, N.F., Patalano, A., Garcia, C.M., Bertoni, J.C., 2017. Use of LSPIV in assessing urban flash flood vulnerability. Natural Hazards 87, 383–394.

Guo, K., Guan, M., Yu, D., 2020. Urban surface water flood modelling – a comprehensive review of current models and future challenges. Hydrology and Earth System Sciences Discussions 2020, 1–27.

Herbich, J.B., Shulits, S., 1964. Large-scale roughness in open-channel flow, in. Proceedings Amercian Society Civil Engineers.

Huang, C.-J., Hsu, M.-H., Teng, W.-H., Wang, Y.-H., 2014. The Impact of Building Coverage in the Metropolitan Area on the Flow Calculation. Water 6, 2449–2466.

Isidoro, J.M.G.P., de Lima, J.L.M.P., Leandro, J., 2013. The study of rooftop connectivity on the rainfall-runoff process by means of a rainfall simulator and a physical model. Zeitschrift für Geomorphologie, Supplementary Issues 57, 177–191.

Kreibich, H., Thaler, T., Glade, T., Molinari, D., 2019. Preface: Damage of natural hazards: assessment and mitigation. Natural Hazards and Earth System Sciences 19, 551–554.

La Loggia, G., Puleo, V., Freni, G., 2020. Floodability: A New Paradigm for Designing Urban Drainage and Achieving Sustainable Urban Growth. Water Resources Management 34.

Le Coz, J., Jodeau, M., Hauet, A., Marchand, B., Le Boursicaud, R., 2014. Image-based velocity and discharge measurements in field and laboratory river engineering studies using the free FUDAA-LSPIV software. In: InProceedings International Conference Fluvial Hydraulics(RiverFlow). Lausanne, Switzerland, pp. 1961–1967.

Leandro, J., Schumann, A., Pfister, A., 2016. A step towards considering the spatial heterogeneity of urban key features in urban hydrology flood modelling. Journal of Hydrology 535, 356–365.

Legout, C., Darboux, F., Nédélec, Y., Hauet, A., Esteves, M., Renaux, B., Denis, H., Cordier, S., 2012. High spatial resolution mapping of surface velocities and depths for shallow overland flow. Earth Surface Processes and Landforms 37, 984–993.

Li, C.W., Zeng, C., 2010. Flow division at a channel crossing with subcritical or supercritical flow. International Journal for Numerical Methods in Fluids 62, 56–73.

Li, X., Erpicum, S., Bruwier, M., Mignot, E., Finaud-Guyot, P., Archambeau, P., Pirotton, M., Dewals, B., 2019. Technical note: Laboratory modelling of urban flooding: strengths and challenges of distorted scale models. Hydrology and Earth System Sciences 23, 1567–1580.

Li, X., Erpicum, S., Mignot, E., Archambeau, P., Rivière, N., Pirotton, M., Dewals, B., 2020. Numerical Insights Into the Effects of Model Geometric Distortion in Laboratory Experiments of Urban Flooding. Water Resources Research 56, e2019WR026774.

Li, X., Kitsikoudis, V., Mignot, E., Archambeau, P., Pirotton, M., Dewals, B., Erpicum, S., 2021. Experimental and numerical study of the effect of model geometric distortion on laboratory modeling of urban flooding. Water Resources Research 57, e2021WR029666.

Lin, J., He, X., Lu, S., Liu, D., He, P., 2020. Investigating the influence of three-dimensional building configuration on urban pluvial flooding using random forest algorithm. Environmental Research, 110438.

Löwe, R., Urich, C., Domingo, N.S., Mark, O., Deletic, A., Arnbjerg-Nielsen, K., 2017. Assessment of urban pluvial flood risk and efficiency of adaptation options through simulations - A new generation of urban planning tools. Journal of Hydrology 550, 355–367.

Luo, H., Fytanidis, D.K., Schmidt, A.R., Garcia, M.H., 2018. Comparative 1D and 3D numerical investigation of open-channel junction flows and energy losses. Advances in Water Resources 117, 120–139.

Martins, R., Rubinato, M., Kesserwani, G., Leandro, J., Djordjevic, S., Shucksmith, J.D., 2018. On the Characteristics of Velocities Fields in the Vicinity of Manhole Inlet Grates During Flood Events. Water Resources Research 54, 6408–6422.
Mejia-Morales, M.A., Mignot, E., Paquier, A., Sigaud, D., Proust, S., 2021. Impact of the porosity of an urban block on the flood risk assessment: A laboratory experiment. Journal of Hydrology 602, 126715.
Mignot, E., Camusson, L., Riviere, N., 2020. Measuring the flow intrusion towards building areas during urban floods: Impact of the obstacles located in the streets and on the facade. Journal of Hydrology 583, 124607.
Mignot, E., Li, X., Dewals, B., 2019. Experimental modelling of urban flooding: A review. Journal of Hydrology 568, 334–342.
Mignot, E., Zeng, C., Dominguez, G., Li, C.-W., Rivière, N., Bazin, P.-H., 2013. Impact of topographic obstacles on the discharge distribution in open-channel bifurcations. Journal of Hydrology 494, 10–19.
Molinari, D., Scorzini, A.R., Arrighi, C., Carisi, F., Castelli, F., Domeneghetti, A., Gallazzi, A., Galliani, M., Grelot, F., Kellermann, P., Kreibich, H., Mohor, G.S., Mosimann, M., Natho, S., Richert, C., Schroeter, K., Thieken, A.H., Zischg, A.P., Ballio, F., 2020. Are flood damage models converging to "reality"? Lessons learnt from a blind test. Natural Hazards and Earth System Sciences 20, 2997–3017.
Muis, S., Güneralp, B., Jongman, B., Aerts, J.C.J.H., Ward, P.J., 2015. Flood risk and adaptation strategies under climate change and urban expansion: A probabilistic analysis using global data. Science of The Total Environment 538, 445–457.
Mustafa, A., Bruwier, M., Archambeau, P., Erpicum, S., Pirotton, M., Dewals, B., Teller, J., 2018. Effects of spatial planning on future flood risks in urban environments. Journal of Environmental Management 225, 193–204.
Mustafa, A., Zhang, X.W., Aliaga, D.G., Bruwier, M., Nishida, G., Dewals, B., Erpicum, S., Archambeau, P., Pirotton, M., Teller, J., 2020. Procedural generation of flood-sensitive urban layouts. Environment and Planning B: Urban Analytics and City Science 47, 889–911.
Muste, M., Fujita, I., Hauet, A., 2008. Large-scale particle image velocimetry for measurements in riverine environments. Water Resources Research 44.
Muste, M., Hauet, A., Fujita, I., Legout, C., Ho, H.-C., 2014. Capabilities of Large-scale Particle Image Velocimetry to characterize shallow free-surface flows. Advances in Water Resources 70, 160–171.
Naves, J., Anta, J., Puertas, J., Regueiro-Picallo, M., SuÃ¡rez, J.,, 2019. Using a 2D shallow water model to assess Large-Scale Particle Image Velocimetry (LSPIV) and Structure from Motion (SfM) techniques in a street-scale urban drainage physical model. Journal of Hydrology 575, 54–65.
Nkwunonwo, U.C., Whitworth, M., Baily, B., 2020. A review of the current status of flood modelling for urban flood risk management in the developing countries. Scientific African 7, e00269.
Paquier, A., Bazin, P.H., EI Kadi Abderrezzak, K., 2020. Sensitivity of 2D hydrodynamic modelling of urban floods to the forcing inputs: lessons from two field cases. Urban Water Journal 17, 457–466.
Peltier, Y., Erpicum, S., Archambeau, P., Pirotton, M., Dewals, B., 2014. Experimental investigation of meandering jets in shallow reservoir. Environmental Fluid Mechanics 14.
Qin, Y., 2020. Urban Flooding Mitigation Techniques: A Systematic Review and Future Studies. Water 12, 3579.
Rosenberger, L., Leandro, J., Pauleit, S., Erlwein, S., 2021. Sustainable stormwater management under the impact of climate change and urban densification. Journal of Hydrology 596, 126137.
Rosenzweig, B.R., Herreros Cantis, P., Kim, Y., Cohn, A., Grove, K., Brock, J., Yesuf, J., Mistry, P., Welty, C., McPhearson, T., Sauer, J., Chang, H., 2021. The value of urban flood modeling. Earth's Future 9, e2020EF001739.
Rubinato, M., Lee, S., Martins, R., Shucksmith, J.D., 2018. Surface to sewer flow exchange through circular inlets during urban flood conditions. Journal of Hydroinformatics 20, 564–576.
Soares-Frazão, S., Zech, Y., 2008. Dam-break flow through an idealised city. Journal of Hydraulic Research 46, 648–658.
Teng, J., Jakeman, A.J., Vaze, J., Croke, B.F.W., Dutta, D., Kim, S., 2017. Flood inundation modelling: A review of methods, recent advances and uncertainty analysis. Environmental Modelling & Software 90, 201–216.
Tesema, D., Abebe, B., 2020. A review of flood modeling methods for urban pluvial flood application. Modeling Earth Systems and Environment.
Testa, G., Zuccala, D., Alcrudo, F., Mulet, J., Soares-Frazão, S., 2007. Flash flood flow experiment in a simplified urban district. Journal of Hydraulic Research 45, 37–44.
Tomiczek, T., Prasetyo, A., Mori, N., Yasuda, T., Kennedy, A., 2016. Physical modelling of tsunami onshore propagation, peak pressures, and shielding effects in an urban building array. Coastal Engineering 117, 97–112.
Varra, G., Pepe, V., Cimorelli, L., Della Morte, R., Cozzolino, L., 2019. On integral and differential porosity models for urban flooding simulation. Advances in Water Resources 136.
Velickovic, M., Zech, Y., Soares-Frazão, S., 2017. Steady-flow experiments in urban areas and anisotropic porosity model. Journal of Hydraulic Research 55, 85–100.
Yin, D., Chen, Y., Jia, H., Wang, Q., Chen, Z., Xu, C., Li, Q., Wang, W., Yang, Y., Fu, G., Chen, A.S., 2021. Sponge city practice in China: A review of construction, assessment, operational and maintenance. Journal of Cleaner Production 280, 124963.
Yin, J., Ye, M., Yin, Z., Xu, S., 2015. A review of advances in urban flood risk analysis over China. Stochastic Environmental Research and Risk Assessment 29, 1063–1070.
Zhi, G., Liao, Z., Tian, W., Wu, J., 2020. Urban flood risk assessment and analysis with a 3D visualization method coupling the PP-PSO algorithm and building data. Journal of Environmental Management 268, 110521.
Zhu, X., Lipeme Kouyi, G., 2019. An Analysis of LSPIV-Based Surface Velocity Measurement Techniques for Stormwater Detention Basin Management. Water Resources Research 55, 888–903.